The Astrophysical Journal, 878:157 (13pp), 2019 June 20 https://doi.org/10.3847/1538-4357/ab21be

On the Formation of Density Filaments in the Turbulent Interstellar Medium

Siyao Xu[1,3], Suoqing Ji[2,4], and A. Lazarian[1]
[1] Department of Astronomy, University of Wisconsin, 475 North Charter Street, Madison, WI 53706, USA; sxu93@wisc.edu, lazarian@astro.wisc.edu
[2] TAPIR & Walter Burke Institute for Theoretical Physics, California Institute of Technology, Pasadena, CA 91125, USA; suoqing@caltech.edu
Received 2017 December 30; revised 2019 April 5; accepted 2019 May 13; published 2019 June 25

Abstract

This study is motivated by recent observations of ubiquitous interstellar density filaments and guided by modern theories of compressible magnetohydrodynamic (MHD) turbulence. The interstellar turbulence shapes the observed density structures. As the fundamental dynamics of compressible MHD turbulence, perpendicular turbulent mixing of density fluctuations entails elongated density structures aligned with the local magnetic field, accounting for low-density parallel filaments seen in diffuse atomic and molecular gas. The elongation of low-density parallel filaments depends on the turbulence anisotropy. When taking into account the partial ionization, we find that the minimum width of parallel filaments in the cold neutral medium and molecular clouds is determined by the neutral–ion decoupling scale perpendicular to magnetic field. In highly supersonic MHD turbulence in molecular clouds, both low-density parallel filaments due to anisotropic turbulent mixing and high-density filaments due to shock compression exist.

Key words: ISM: magnetic fields – ISM: structure – turbulence

1. Introduction

Observations reveal that filamentary density structures widely spread in the interstellar medium (ISM), including both diffuse media (e.g., McClure-Griffiths et al. 2006; Clark et al. 2014; Kalberla et al. 2016; Planck Collaboration et al. 2016a) and highly fragmented molecular clouds (MCs; e.g., Schneider & Elmegreen 1979; Williams et al. 2000; André et al. 2010). Moreover, low-density filaments in diffuse media and diffuse regions of MCs preferentially align with the magnetic field, whereas dense filaments in MCs tend to be perpendicular to the magnetic field (Goldsmith et al. 2008; Kalberla et al. 2016; Planck Collaboration et al. 2016a, 2016b). The former provides the information on the interstellar magnetic field. The latter is important for understanding the star formation process, as dense filaments in MCs coincide with birthplaces of protostellar cores (André et al. 2014; Könyves et al. 2015; Marsh et al. 2016). Besides its significance in interstellar processes, H I filaments parallel to magnetic fields can also be useful for studies of cosmic microwave background polarization (Clark et al. 2015).

As the ISM is turbulent (Armstrong et al. 1995; Chepurnov & Lazarian 2010), understanding the turbulence properties is essential for explaining the magnetic field and density structures in the ISM. Important strides have been made toward advancing the theories of magnetohydrodynamic (MHD) turbulence concerning, e.g., the dynamics and statistics of MHD turbulence (Goldreich & Sridhar 1995; hereafter GS95; Lazarian & Vishniac 1999; hereafter LV99), MHD turbulence in a compressible medium (Lithwick & Goldreich 2001; henceforth LG01; Cho & Lazarian 2002, 2003) and in a partially ionized medium (LG01; Lazarian et al. 2004; Xu et al. 2015, 2016), and their numerical testing (Maron & Goldreich 2001; Cho et al. 2002; Kowal et al. 2009, 2012). With a general applicability in essentially all branches of astrophysics involving fluid dynamics (McKee & Ostriker 2007), the theoretical developments of MHD turbulence provide new insights in many long-standing problems (e.g., Yan & Lazarian 2002; Lazarian & Yan 2014; Xu & Lazarian 2017a; Xu & Zhang 2017a, 2017b). In particular, the turbulent reconnection of magnetic fields inherent in MHD turbulence (LV99) was introduced to resolve the magnetic flux problem in star formation (Lazarian 2005; Santos-Lima et al. 2010; Lazarian et al. 2012), and the turbulence anisotropy has been employed to develop a new velocity gradient technique for measuring interstellar magnetic fields (González-Casanova & Lazarian 2017; Yuen & Lazarian 2017b; Lazarian & Yuen 2018).

In the multiphase ISM, the interstellar turbulence induces density fluctuations and influences density structures in different phases. In diffuse warm phases, the turbulence is subsonic to transonic (Hill et al. 2008; Chepurnov et al. 2010; Gaensler et al. 2011; Burkhart et al. 2012), while the turbulence in dense cold phases is supersonic (Zuckerman & Evans 1974; Zuckerman & Palmer 1974; Larson 1981; Heyer & Brunt 2004). In accordance with distinctive turbulence regimes, we naturally expect that the resultant density structures differ in different phases. This has been confirmed by statistical studies of turbulent densities (Beresnyak et al. 2005; Kowal et al. 2007; Lazarian et al. 2008; Burkhart et al. 2009, 2010; Collins et al. 2012; Federrath & Klessen 2012; Burkhart et al. 2015a). In compressible MHD turbulence, density fluctuations are passively regulated by Alfvénic modes, which are responsible for the dynamics of MHD turbulence, and thus present the same statistical features as turbulent velocities (LG01, Cho & Lazarian 2003). But when the compressible MHD turbulence is highly supersonic, besides the density fluctuations associated with Alfvén modes, shocks driven by supersonic turbulent flows can produce additional density structures, which are characterized by large density contrasts on small scales due to the shock compression. The fact of different density structures arising in different turbulence regimes in the multiphase ISM has been shown by overwhelming observations (see, e.g., Armstrong et al. 1995; Chepurnov & Lazarian 2010; reviews by Lazarian 2009; Hennebelle & Falgarone 2012 and references therein), and has been applied by Xu & Zhang (2016, 2017b) to modeling the Galactic electron density

[3] Hubble Fellow.
[4] Sherman Fairchild Fellow.

fluctuations and interpreting interstellar rotation measure fluctuations and scattering measurements of pulsars.

In this paper, based on the established and numerically tested theories of compressible MHD turbulence, we will investigate the physical origin of density filaments in the multiphase ISM. In Section 2, we introduce the properties of compressible MHD turbulence in the ISM. In Section 3, we focus on the formation mechanism of low-density parallel filaments in both subsonic and supersonic interstellar turbulence, and present both the analytical theory and numerical tests. In Section 4, we briefly discuss the formation mechanism of dense filaments in the supersonic turbulence of MCs. The further discussion and summary follow in Sections 5 and 6, respectively.

2. MHD Turbulence in the Multiphase ISM

The ISM is compressible. Theories of incompressible strong MHD turbulence (GS95; LV99) have been extended for studying compressible MHD turbulence, on the basis that (1) the solenoidal Alfvénic component of turbulent velocities dominates over the compressible component (Balsara & Pouquet 1999; Cho & Lazarian 2002; Kowal & Lazarian 2010); (2) the Alfvénic component remains incompressible and is only marginally coupled with compressible slow and fast modes (LG01; Cho & Lazarian 2002, 2003); (3) slow modes passively follow the cascade of Alfvén modes and thus have the same anisotropic scaling as Alfvén modes, while fast modes independently have an isotropic scaling (LG01; Cho & Lazarian 2002, 2003). Both theoretical arguments (LG01) and numerical evidence by decomposing compressible MHD turbulence into Alfvén, slow, and fast modes (Cho & Lazarian 2002, 2003) justify the validity of the scaling and anisotropy of Alfvénic turbulence in a compressible medium.

In the multiphase ISM with dramatically varying temperatures, the compressible MHD turbulence can be subsonic or supersonic in different interstellar phases.

(1) Subsonic to transonic warm ionized medium (WIM) and warm neutral medium (WNM).

The sonic Mach number $\mathcal{M}_s$ is defined as the ratio of the turbulent speed at the driving scale of turbulence to the sound speed. $\mathcal{M}_s \lesssim 1$ measured in the WIM (Kulkarni & Heiles 1987; Haffner et al. 1999; Hill et al. 2008; Gaensler et al. 2011; Burkhart et al. 2012) and in the WNM (Chepurnov et al. 2010) indicates that the turbulence in these diffuse warm phases is subsonic to transonic. In compressible MHD turbulence with $\mathcal{M}_s$ of the order of unity, slow modes are passively mixed by Alfvénic turbulent velocities (LG01). Therefore, density fluctuations resulting from slow modes are dictated by the dynamics of Alfvén modes and obey the same scaling as Alfvén modes. The same Kolmogorov spectrum of density fluctuations as that of velocity fluctuations has been confirmed by MHD simulations (e.g., Cho & Lazarian 2003). Observations of the WIM reveal a "big power law in the sky" of electron density fluctuations spanning from 10^6 m to hundreds of parsecs, which is consistent with the Kolmogorov scaling (Armstrong et al. 1995; Chepurnov & Lazarian 2010).

(2) Supersonic cold neutral medium (CNM) and MCs.

The turbulence in colder and denser phases are supersonic with $\mathcal{M}_s > 1$ (Zuckerman & Palmer 1974; Larson 1981; Chepurnov et al. 2010). In highly supersonic MHD turbulence, density fluctuations are subjected to not only the Alfvénic mixing, but also the shock compression. The former acts to smooth the density variation, whereas the latter produces large density contrasts and results in a shallow density spectrum with a significant excess of high-density structures at small scales. Such shallow density spectra have been confirmed by supersonic MHD simulations (Beresnyak et al. 2005; Kowal et al. 2007), and also measured in the CNM and MCs (Lazarian 2009; Hennebelle & Falgarone 2012). Importantly, we note that even in highly supersonic MHD turbulence, the turbulence dynamics is still dominated by Alfvén modes. Different from the density spectrum, the spectrum of velocity fluctuations in supersonic MHD turbulence does not significantly deviate from the Kolmogorov scaling (Kowal & Lazarian 2010). Turbulent velocities measured in the low-density region of an MC exhibit a Kolmogorov spectrum (Qian et al. 2018).

The different density structures in the subsonic to transonic turbulence of diffuse warm phases and in the supersonic turbulence of dense cold phases hold the key to understanding a variety of phenomena in the ISM, e.g., the interstellar scattering of Galactic pulsars (Xu & Zhang 2017b) and interstellar rotation measure fluctuations (Xu & Zhang 2016), as well as the density filaments in the ISM. In what follows we first focus on the formation mechanism of low-density filaments based on the dynamics of Alfvén modes in both subsonic and supersonic interstellar turbulence (Section 3). Then we briefly discuss the formation of dense filaments in highly supersonic interstellar turbulence (Section 4).

3. Formation of Low-density Parallel Filaments in Both Subsonic and Supersonic Interstellar Turbulence

3.1. Perpendicular Turbulent Mixing and Low-density Parallel Filaments

In Alfvénic turbulence, the turbulent mixing of magnetic fields takes place in the direction perpendicular to the local magnetic field, which is enabled by the turbulent reconnection of magnetic fields (LV99). This perpendicular turbulent mixing results in the scale-dependent anisotropy of MHD turbulence and makes the essential distinction between MHD and hydrodynamic turbulence.

The turbulent energy injected at a large scale, i.e., the injection scale L, progressively cascades down to small scales. The nonlinear cascade rate of Alfvénic turbulence, i.e., the eddy-turnover rate, determines the perpendicular turbulent mixing rate,

$$\tau_{cas}^{-1} = v_l l_\perp^{-1} = V_{st} L_{st}^{-\frac{1}{3}} l_\perp^{-\frac{2}{3}}, \quad (1)$$

with the local turbulent velocity v_l at the length scale $l_\perp$ measured in the direction perpendicular to the local magnetic field. The critical balance between τ_{cas}^{-1} and the frequency of Alfvén waves propagating along the magnetic field is satisfied in the strong MHD turbulence regime (GS95). In the above expression, the GS95 scaling for the strong MHD turbulence is used:

$$v_l = V_{st} (l_\perp / L_{st})^{\frac{1}{3}}, \quad (2)$$

where V_{st} is the turbulent velocity at the injection scale L_{st} of strong MHD turbulence. More specifically, in super-Alfvénic turbulence with dominant turbulent kinetic energy at L, there is

$$V_{st} = V_A,\ L_{st} = L\mathcal{M}_A^{-3}, \quad (3)$$

where V_A is the Alfvén speed, $\mathcal{M}_A = V_L/V_A > 1$ is the Alfvén Mach number, and V_L is the turbulent velocity at L. Within the

range [L, $L_{\rm st}$], the turbulence is in the hydrodynamic regime with isotropic turbulent mixing and isotropic scaling. In the case of sub-Alfvénic turbulence with dominant magnetic energy at L, i.e., $\mathcal{M}_{\rm A} < 1$, there is (Lazarian 2006),

$$V_{\rm st} = V_L \mathcal{M}_{\rm A},\ L_{\rm st} = L\mathcal{M}_{\rm A}^2. \tag{4}$$

Within [L, $L_{\rm st}$], it is the weak turbulence resulting from weakly interacting Alfvén waves (LV99).

Given the expression of the perpendicular mixing rate (Equation (1)), the critical balance condition

$$\tau_{\rm cas}^{-1} = V_{\rm A}/l_{\parallel} \tag{5}$$

leads to the anisotropic scaling relation of strong MHD turbulence,

$$l_{\parallel} = \frac{V_{\rm A}}{V_{\rm st}} L_{\rm st}^{\frac{1}{3}} l_{\perp}^{\frac{2}{3}}, \tag{6}$$

where $l_{\parallel}$ is length scale measured parallel to the magnetic field. It shows that the anisotropy of strong MHD turbulence is scale-dependent, with smaller-scale turbulent eddies more elongated along the magnetic field.

As mentioned above, slow modes that induce density fluctuations do not affect the dynamics of MHD turbulence. The perpendicular mixing of density fluctuations by Alfvén modes is analogous to the mixing of a passive scalar (LG01). The resulting density fluctuations follow the same cascade and conform to the same anisotropic scaling as Alfvénic turbulent velocities. Shaped by the turbulence anisotropy, density fluctuations tend to exhibit elongated structures along the magnetic field, i.e., parallel density filaments.

After the injection of a density source $\delta n(l_0)$, as the turbulent mixing operates toward the homogenization of density variations, lower-density fluctuations develop on length scales below the density injection scale l_0 with the scaling

$$\delta n(l_{\perp}) = \delta n(l_0)(l_{\perp}/l_0)^{\frac{1}{3}}. \tag{7}$$

Thus we expect that parallel filaments formed in MHD turbulence tend to have a relatively low density contrast. Following the turbulent energy cascade, the lifetime of a parallel filament is determined by the turnover time of the turbulent eddy at the perpendicular length scale equal to the filament width.

3.2. Numerical Tests on the Formation Mechanism of Low-density Parallel Filaments

We perform 3D simulations of driven MHD turbulence as numerical tests for the above theory. The FLASH code (Fryxell et al. 2000) is deployed, with a directionally unsplit staggered mesh (USM) MHD solver based on a finite-volume, high-order Godunov method combined with a constrained transport (CT) type scheme (Tzeferacos et al. 2012; Lee 2013), to solve the equations of inviscid ideal magnetohydrodynamics as follows:

$$\frac{\partial \rho}{\partial t} + \nabla \cdot (\rho \boldsymbol{v}) = 0 \tag{8a}$$

$$\frac{\partial \rho \boldsymbol{v}}{\partial t} + \nabla \cdot (\rho \boldsymbol{v}\boldsymbol{v} - \boldsymbol{B}\boldsymbol{B}) + \nabla p_* = \boldsymbol{s}_{\rm stir} \tag{8b}$$

$$\frac{\partial \boldsymbol{B}}{\partial t} + \nabla \cdot (\boldsymbol{v}\boldsymbol{B} - \boldsymbol{B}\boldsymbol{v}) = 0 \tag{8c}$$

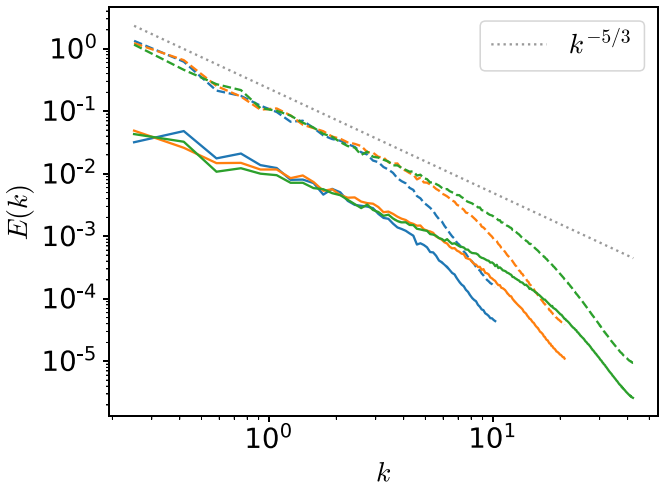

Figure 1. Energy power spectra of density fluctuations (solid lines) and velocity fluctuations (dashed lines) from snapshots at $t \sim 6\ t_{{\rm eddy},L}$ with different resolutions: blue—resolution of 128^3, orange—resolution of 256^3, and green—resolution of 512^3. The slope of Kolmogorov spectrum $k^{-5/3}$ is indicated by the dotted gray line.

$$\nabla \cdot \boldsymbol{B} = 0 \tag{8d}$$

where $p_* = p + B^2/(8\pi)$ is the total pressure including both gas pressure p and magnetic pressure $B^2/(8\pi)$, and $\boldsymbol{s}_{\rm stir}$ is the source term of stirring. The isothermal condition is applied during the evolution of these governing equations.

Our simulations are performed in a 3D Cartesian box with the size of $L_{\rm box} = 10$ along each dimension and the resolutions of 128^3, 256^3, and 512^3. To examine the effect of turbulent mixing on density fluctuations, we adopt the solenoidal driving of turbulence, which does not generate density structures associated with compressible modes. The stirring is performed over wavenumbers of $1 \leqslant n \leqslant 4$, which corresponds to the k vector of $0.1 \leqslant k \equiv n/L_{\rm box} \leqslant 0.4$ and the length scale of $2.5 \leqslant l \equiv k^{-1} \leqslant 10$, with a driving amplitude of paraboloidal shape in Fourier space and an autocorrelation time of $t_{\rm correlation} \equiv L_{\rm box}/2V = 5$, where $V = 1$ is the rms velocity when the simulations reach a statistically stable state (Federrath et al. 2010). The simulations are initialized with a uniform density and sound speed, and constant magnetic fields along the x-axis. These initial values are carefully chosen in order that after stirring over a certain period (~a few largest eddy-turnover time $t_{{\rm eddy},L} = L/V$), the simulations become statistically stable at $\mathcal{M}_{\rm s} \sim 0.5$ and $\mathcal{M}_{\rm A} \sim 1$, where the sonic- and Alfvén–Mach numbers are rms values averaged over the entire box. These values are typical for the subsonic diffuse warm medium with comparable turbulent and magnetic energies at the driving scale of turbulence (Beck et al. 1996).

Figure 1 presents the energy spectra of both density fluctuations $\rho/\bar{\rho}$ (density normalized by mean density $\bar{\rho}$) and velocity fluctuations (velocity magnitude normalized by sound speed), from the snapshot of $t \sim 6\ t_{{\rm eddy},L}$. As expected, density fluctuations passively follow the same cascade as turbulent velocities, and as a result, the density spectrum exhibits the same Kolmogorov form as that of the velocity spectrum. In addition, these spectra demonstrate a nice convergence within available inertial range in each of the simulations with different resolutions. Hereinafter, we focus on the simulations with the highest resolution of 512^3 for our analysis.

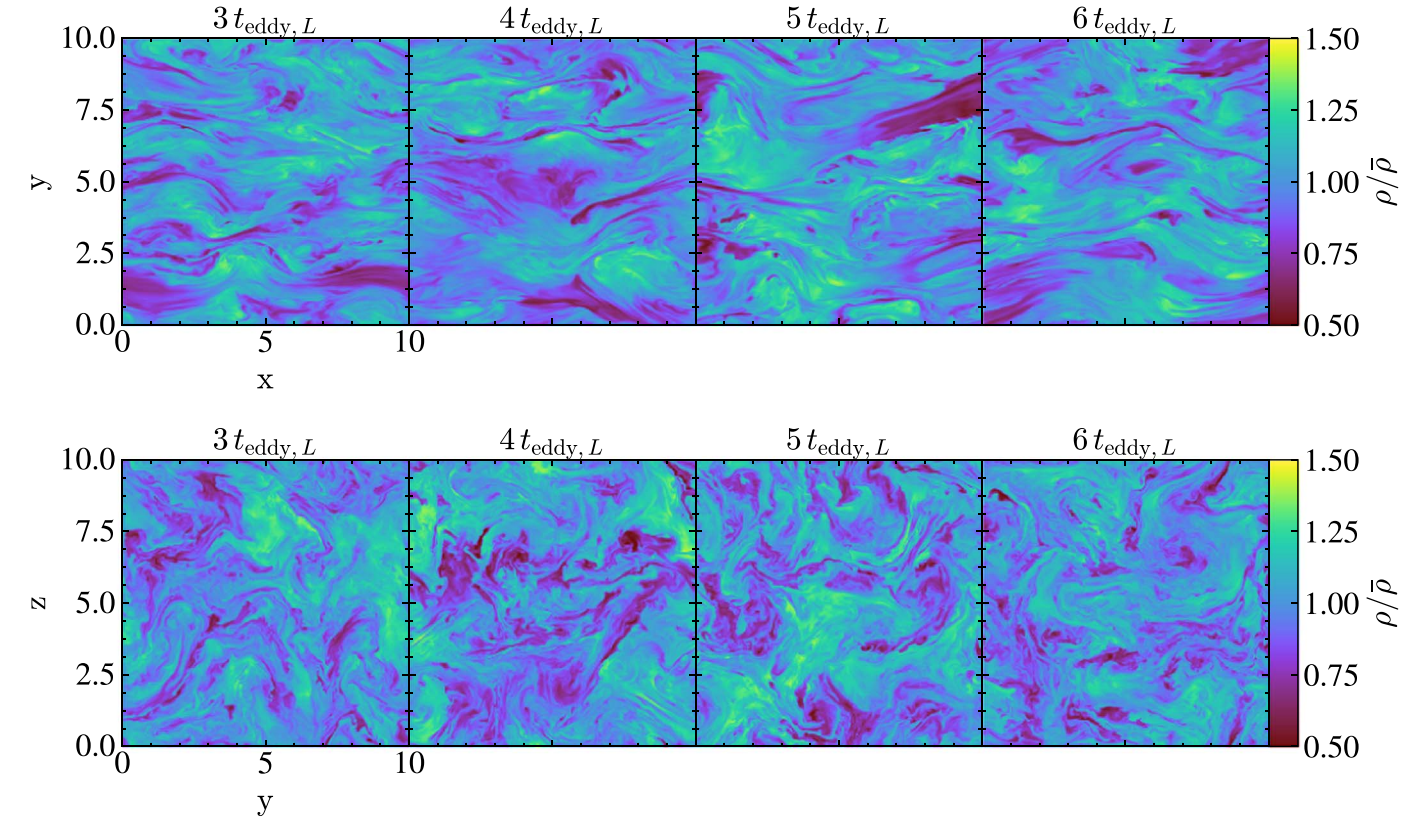

(a)

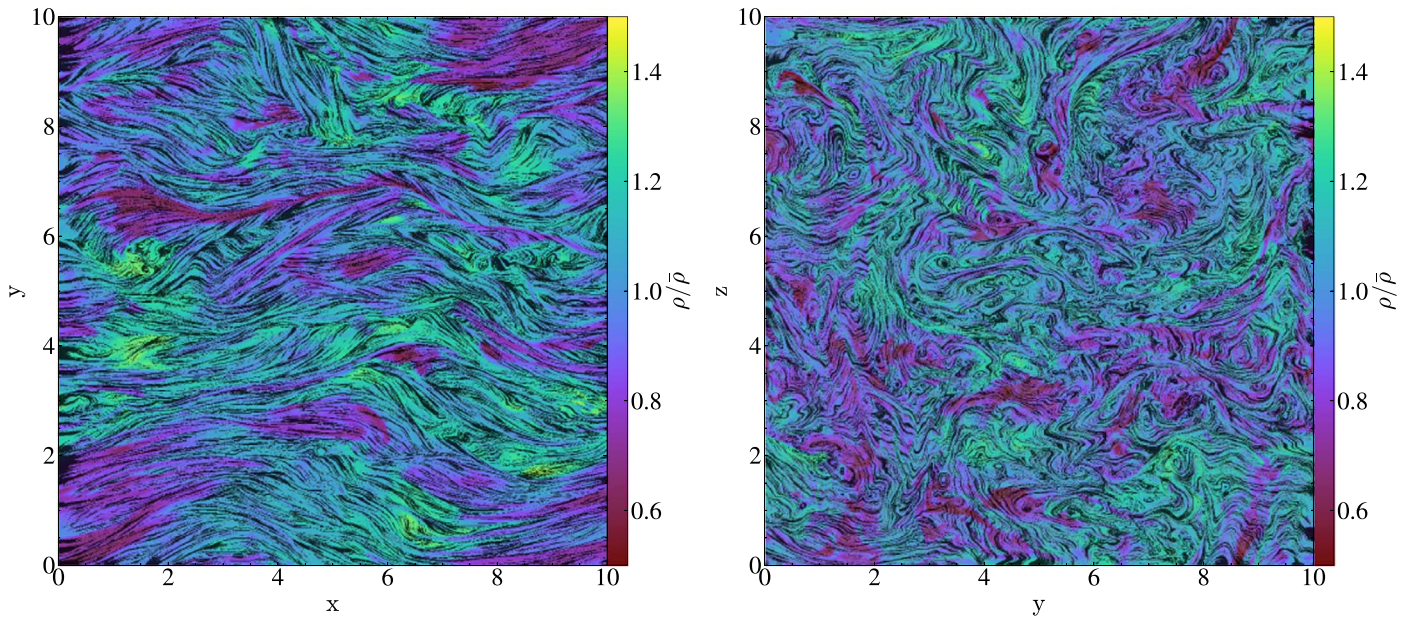

(b)

Figure 2. Structures of density fluctuations and magnetic fields. (a) Slice plots of density fluctuations at different times, viewed along the z-axis (upper panel) and x-axis (lower panel). (b) Slice plots of density fluctuations superposed with magnetic field lines at $t = 6t_{\rm eddy,L}$, viewed along the z-axis (left panel) and x-axis (right panel).

To numerically test the perpendicular turbulent mixing of density fluctuations, at $t = 3t_{\rm eddy,L}$ when the simulation becomes statistically stable, we assign certain regions with a dimensionless "dye" value of $f_{\rm dye} = 1$, which is a mass scalar passively advected with density: $\partial_t(f_{\rm dye}\,\rho) + \nabla \cdot (f_{\rm dye}\,\rho \boldsymbol{v}) = 0$, and trace the time evolution of its spatial configuration. In Figures 2 and 3, we show the slice plots of the gas density fluctuations $\rho/\bar{\rho}$ and dyed density fluctuations $f_{\rm dye}\,\rho/\bar{\rho}$ at different times, as well as the magnetic field geometries, viewed along the z-axis and x-axis respectively. Note that the

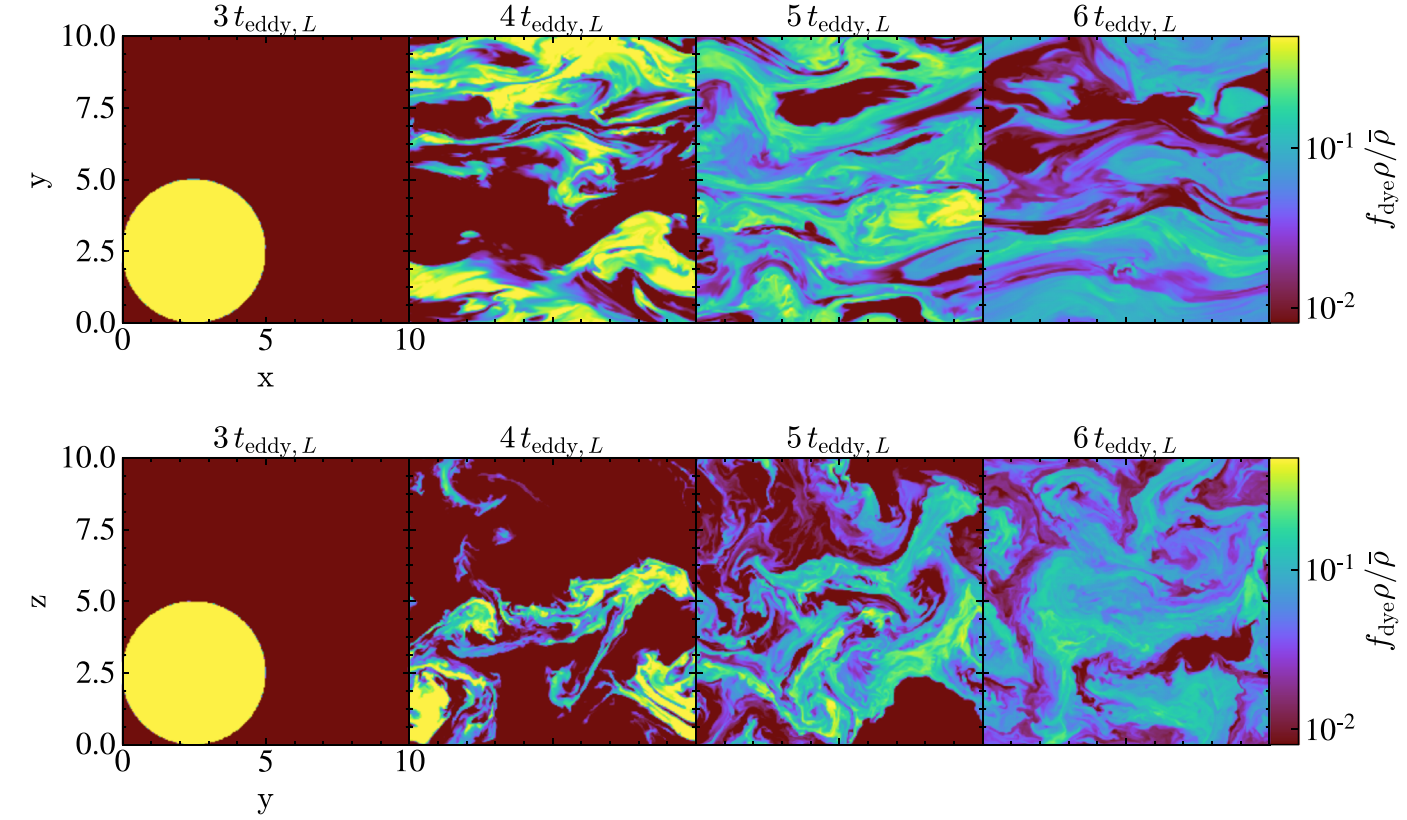

(a)

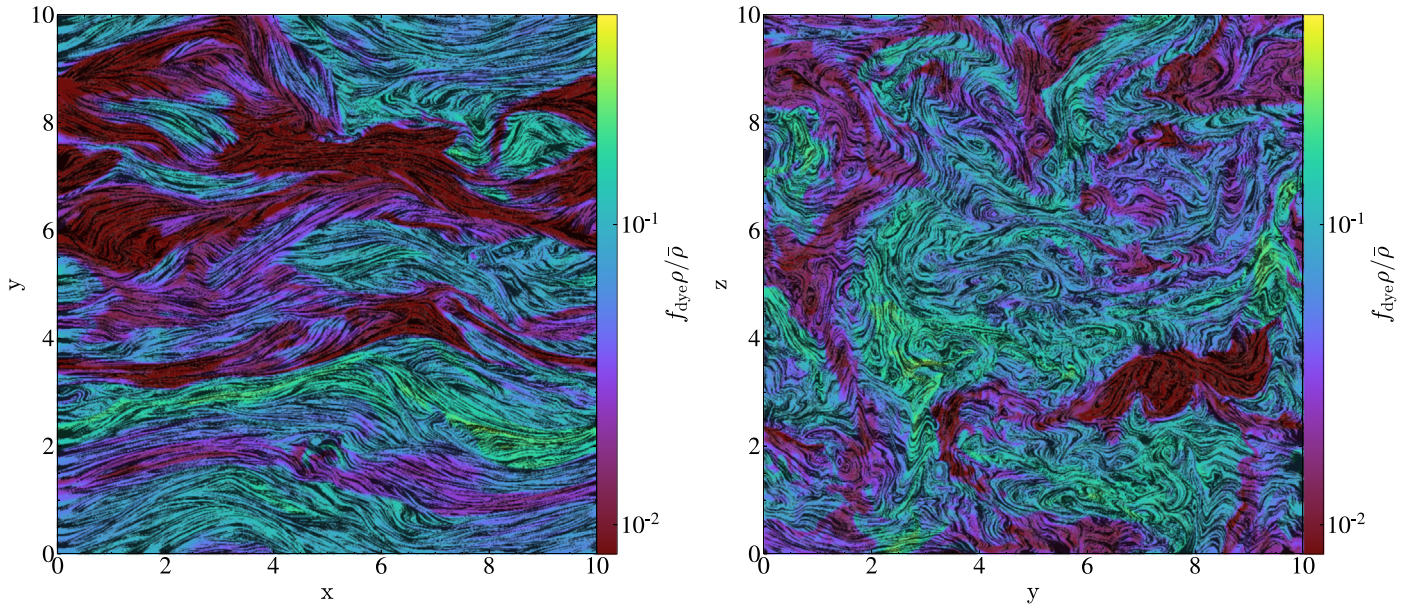

(b)

Figure 3. Structures of dyed density fluctuations and magnetic fields. (a) Slice plots of dyed density fluctuations at different times, viewed along the z-axis (upper panel) and x-axis (lower panel). (b) Slice plots of dyed density fluctuations superposed with magnetic field lines at $t = 6t_{\mathrm{eddy},L}$, viewed along the z-axis (left panel) and x-axis (right panel).

magnetic field lines are initially aligned along the x-axis. When the simulation is statistically stable, we find $\langle|\delta B|\rangle/\bar{B} \sim 0.7$, where δB is the magnetic field perturbation, $\bar{B}$ is the mean magnetic field, and $\langle ...\rangle$ denotes an ensemble average. In a situation with $\langle|\delta B|\rangle/\bar{B} > 1$, we do not expect to see significantly different magnetic field and density structures at different line-of-sight orientations.

In Figure 3, from the snapshots of density fluctuations taken at different times we see that under the effect of perpendicular turbulent mixing, the initial dyed density fluctuations with an

isotropic spatial distribution evolves into smaller-scale anisotropic density structures with lower density variations. The resulting small-scale density structures are highly elongated along the local magnetic field direction.

The perpendicular turbulent mixing leads to the scale-dependent anisotropy of MHD turbulence. In Figure 4, we display the slice plots of density fluctuations measured within different ranges of length scales. To quantify the scale-dependent anisotropy, we overplot rectangles indicating the scaling relation in Equation (6) at $k = 0.45$, 1.95, and 3.95, with $l_\perp \approx k^{-1}$, $V_{\rm st} = V_A$, and $L_{\rm st} = L = 4$ where the energy injection peaks. We see that the theoretical scaling well describes the anisotropy of density structures, which becomes stronger toward smaller scales. By comparing with the similar measurements of turbulent velocities in Figure 5, we see the same scale-dependent anisotropy of both velocity and density fluctuations as expected. The elongated velocity and density structures are both well aligned with the local magnetic field.

As the density fluctuations in turbulence tend to spread out in k space (see Figure 3), we further present the density fluctuations extending over a broader range of length scales within the inertial range of turbulence in Figure 6. We see that the density structures appear to be more coherent and elongated along magnetic field lines due to the superposition of density fluctuations on different length scales. Therefore, in a realistic situation involving multiscale density fluctuations, we expect to see more extended filamentary density structures in magnetized turbulence.

The above numerical tests confirm that the perpendicular turbulent mixing in MHD turbulence can account for the formation of low-density filaments parallel to magnetic fields. We caution that due to the limited numerical resolution, the inertial range of turbulence in MHD simulations is quite small compared with that of the interstellar turbulence (Armstrong et al. 1995; Chepurnov & Lazarian 2010). According to Equation (6), the degree of turbulence anisotropy depends on the separation between $L_{\rm st}$ and $l_\perp$,

$$\frac{l_\parallel}{l_\perp} = \frac{V_{\rm A}}{V_{\rm st}}\left(\frac{L_{\rm st}}{l_\perp}\right)^{\frac{1}{3}}. \quad (9)$$

It means that the low-density parallel filaments in the ISM can be much more elongated than those observed in simulations. Moreover, as turbulent mixing tends to homogenizes the density distribution, multiphase turbulence simulations are necessary for generating prominently visible parallel filaments (Kritsuk & Norman 2004).

3.3. Low-density Parallel Filaments in a Partially Ionized Medium

The ISM is commonly partially ionized (Draine 2011). The coupling state between neutrals and ions depends on the length scale of interest. If the MHD turbulence cascades down to sufficiently small scales where the two-fluid effect is important, we should consider the decoupling between neutrals and ions when studying the density structure of neutral gas.

The parallel neutral–ion decoupling scale is defined as

$$l_{\rm ni,dec,\parallel} = \frac{V_{\rm A}}{\nu_{\rm ni}}, \quad (10)$$

corresponding to the equalization between the Alfvén wave frequency and the neutral–ion collision frequency $\nu_{\rm ni} = \gamma_d\, \rho_i$, where γ_d is the drag coefficient (see, e.g., Shu 1992), and ρ_i is the ion mass density. According to the anisotropic scaling of Alfvénic turbulence (Equation (6)), the perpendicular neutral–ion decoupling scale is,

$$l_{\rm ni,dec,\perp} = \nu_{\rm ni}^{-\frac{3}{2}} L_{\rm st}^{-\frac{1}{2}} V_{\rm st}^{\frac{3}{2}}. \quad (11)$$

Since the ion–neutral collisional damping of Alfvénic turbulence is weak when the neutral–ion coupling is strong (Xu et al. 2015, 2016; Xu & Lazarian 2017b), here we consider that the damping effect is insignificant on length scales down to $l_{\rm ni,dec,\perp}$ and thus apply the anisotropic scaling of quasi-single-fluid Alfvénic turbulence to determine $l_{\rm ni,dec,\perp}$. On scales larger than $l_{\rm ni,dec,\perp}$, the strongly coupled neutrals and ions together carry the anisotropic MHD turbulence, and density fluctuations present a filamentary structure along the magnetic field due to the perpendicular turbulent mixing as discussed above. On smaller scales, neutrals decouple from ions and the magnetic field. Therefore they independently carry the isotropic hydrodynamic turbulence (Burkhart et al. 2015b; Xu et al. 2015). In the case when the viscous damping scale of turbulence is sufficiently small, the cascade of MHD turbulence in neutrals terminates at $l_{\rm ni,dec,\perp}$, which is thus the minimum width of low-density parallel filaments in the neutral gas. We note that due to the turbulent energy cascade and turbulent mixing of density fluctuations, the density fluctuations at $l_{\rm ni,dec,\perp}$ are relatively low, and thus we do not expect that $l_{\rm ni,dec,\perp}$ characterizes a typical scale of density structures.

We should stress that the "ambipolar diffusion (AD) length" frequently adopted in the literature (e.g., Mouschovias 1991; Balsara 1996; Ntormousi et al. 2016) is in fact $l_{\rm ni,dec,\parallel}$ in Equation (10). Its formulation is based on a linear description of Alfvén waves. For the nonlinear anisotropic Alfvénic turbulence, only $l_{\rm ni,dec,\perp}$ in Equation (11) is relevant (Xu et al. 2015, 2016). The disparity between $l_{\rm ni,dec,\parallel}$ and $l_{\rm ni,dec,\perp}$ can be quite large especially in sub-Alfvénic turbulence. The latter is difficult to resolve numerically due to the limited numerical resolution. The two-fluid MHD simulations by Burkhart et al. (2015b) showed evidence for the existence of Alfvénic turbulence on scales below $l_{\rm ni,dec,\parallel}$. More high-resolution two-fluid numerical tests on the behavior of MHD turbulence at $l_{\rm ni,dec,\parallel}$ and $l_{\rm ni,dec,\perp}$ are necessary.

To illustrate the filamentary structure in the partially ionized ISM, we adopt the typical driving conditions of the interstellar turbulence, $L = 30$ pc, $V_L = 10\,{\rm km\,s^{-1}}$, and typical parameters of the WNM, the CNM, and MCs (Draine & Lazarian 1998; see Table 1). Besides, we use $\gamma_d = 5.5 \times 10^{14}\,{\rm cm^3 g^{-1} s^{-1}}$, the ion and neutral masses $m_{\rm i} = m_{\rm n} = m_{\rm H}$ for the WNM and the CNM, and $\gamma_d = 3.5 \times 10^{13}\,{\rm cm^3 g^{-1} s^{-1}}$, $m_{\rm i} = 29 m_{\rm H}$, and $m_{\rm n} = 2.3 m_{\rm H}$ for MCs (Draine et al. 1983; Shu 1992), where $m_{\rm H}$ is the mass of the hydrogen atom.

In the case of the WNM, given the above parameters, the turbulence is sub-Alfvénic. The viscous damping scale

$$l_{\nu,\perp} = \nu_n^{\frac{3}{4}} L^{\frac{1}{4}} V_L^{-\frac{3}{4}} M_{\rm A}^{-\frac{1}{4}}, \quad (12)$$

is larger than $l_{\rm ni,dec,\perp}$, where $\nu_n = v_{\rm th}/(n_n\, \sigma_{nn})$ is the viscosity in neutrals, with the neutral thermal speed $v_{\rm th}$, the neutral number density n_n, and the cross-section of a neutral–neutral collision $\sigma_{nn} \sim 10^{-14}\,{\rm cm^2}$ (Vranjes & Krstic 2013). This means that the sub-Alfvénic turbulence in the WNM is damped due to

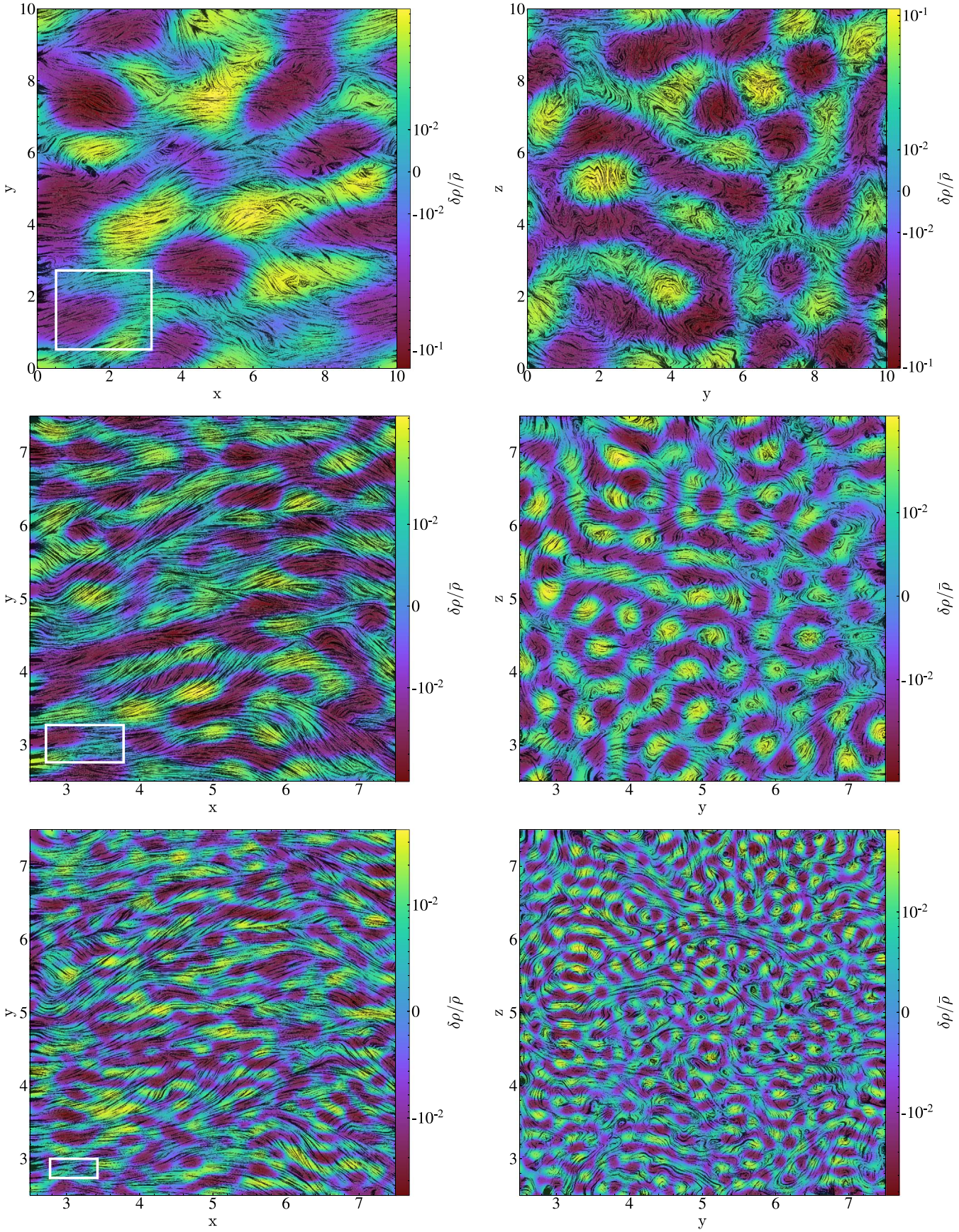

Figure 4. Slice plots of density fluctuations at $t = 6t_{\mathrm{eddy},L}$, superposed with magnetic field lines. Upper panel: $0.45 < k < 0.55$; middle panel: $1.95 < k < 2.05$; lower panel: $3.95 < k < 4.05$; left panel: viewed along z-axis; right panel: viewed along x-axis. The figures in the middle and lower panels are zoomed in by a factor of 2. The rectangles giving the theoretical predictions (Equation (6)) for the anisotropic scaling of density structures at $k = 0.45$, 1.95, and 3.95 are overplotted.

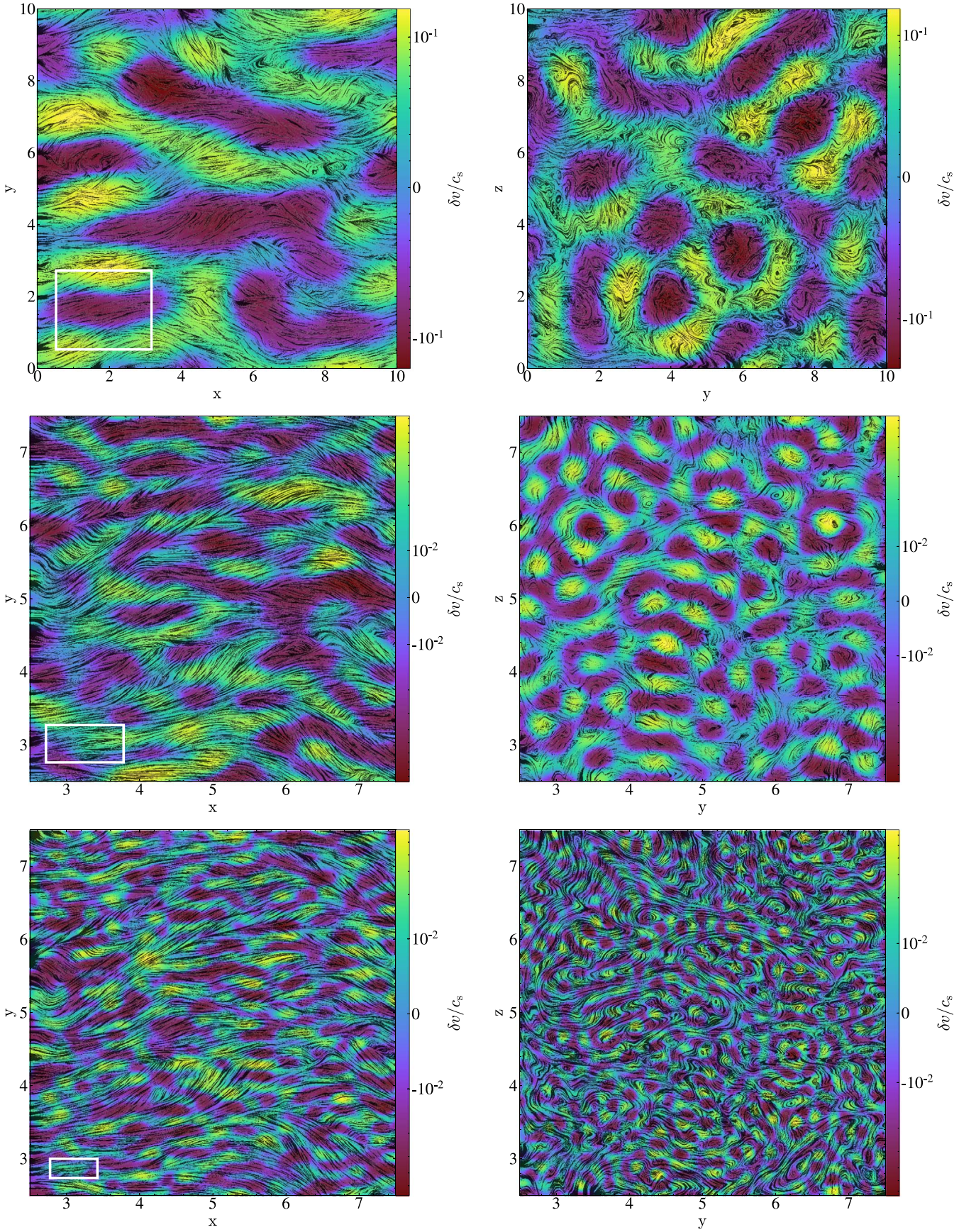

Figure 5. Same as Figure 4 but for velocity fluctuations.

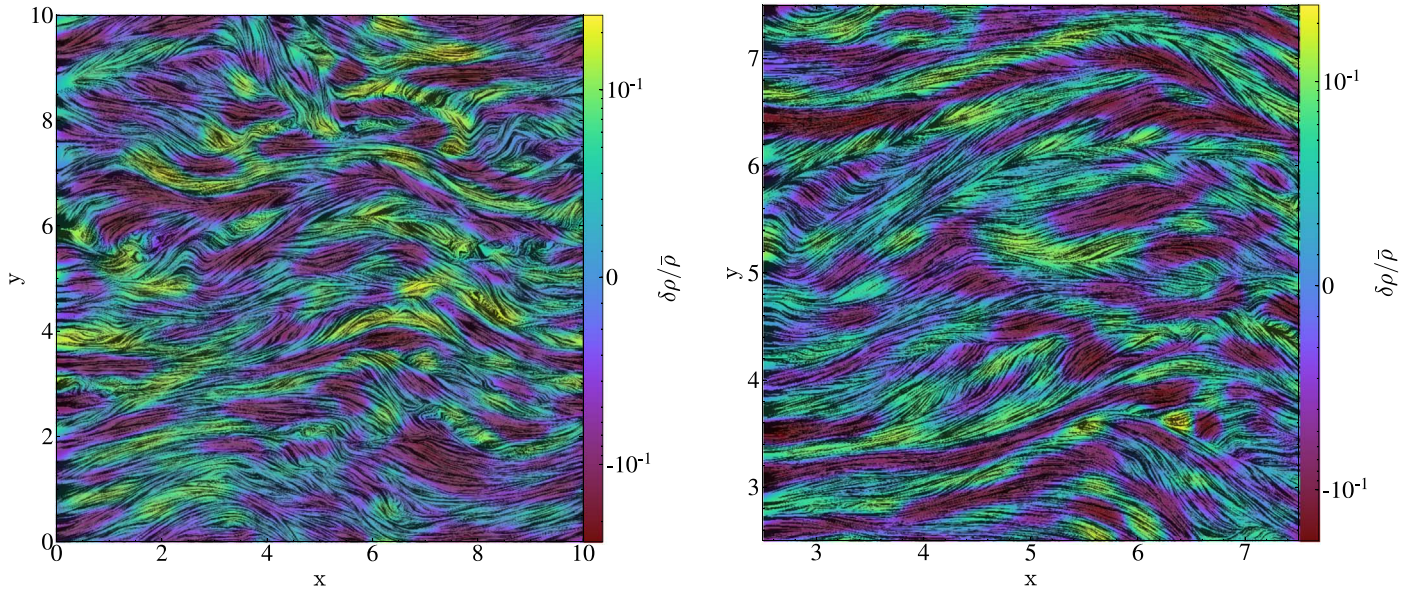

Figure 6. Same as Figure 4 but for a broader range of k. Left: $1 < k < 2$; right: $2 < k < 4$, viewed along the z-axis.

neutral viscosity when ions and neutrals are strongly coupled (Lazarian et al. 2004; Xu et al. 2016). So the density structure of both neutral and ionized gases at $l_{\nu,\perp}$ exhibit the anisotropy of MHD turbulence. To quantify the elongation of the viscous-scale density filament, we calculate the axial ratio as (Equations (4), (9) and (12), Table 1)

$$A_{\nu,\mathrm{sub}} = \frac{l_{\nu,\parallel}}{l_{\nu,\perp}} = \nu_n^{-\frac{1}{4}} L^{\frac{1}{4}} V_L^{\frac{1}{4}} M_{\mathrm{A}}^{-\frac{5}{4}}, \tag{13}$$

which reflects the local turbulence anisotropy and has a large value in the sub-Alfvénic WNM.

In cases of the CNM and MCs, with the above parameters adopted, the turbulence turns out to be super-Alfvénic. Different from the WNM, there is $l_{\mathrm{ni,dec},\perp} > l_{\nu,\perp}$ in the CNM and MCs, so the effect of neutral–ion decoupling on MHD turbulence is important. To determine the neutral–ion decoupling scale, we can rewrite Equation (11) by using Equation (3),

$$l_{\mathrm{ni,dec},\perp,\mathrm{sup}} = \nu_{\mathrm{ni}}^{-\frac{3}{2}} L^{-\frac{1}{2}} V_L^{\frac{3}{2}}, \tag{14}$$

which is independent of the magnetic field strength. The axial ratio at the decoupling scale is (Equations (10) and (14))

$$A_{\mathrm{dec,\ sup}} = \frac{l_{\mathrm{ni,dec},\parallel}}{l_{\mathrm{ni,dec},\perp,\mathrm{sup}}} = \nu_{\mathrm{ni}}^{\frac{1}{2}} L^{\frac{1}{2}} V_L^{-\frac{1}{2}} \mathcal{M}_{\mathrm{A}}^{-1}. \tag{15}$$

The reason for the small $A_{\mathrm{dec,sup}}$ in a highly super-Alfvénic MC is that with comparable turbulent and magnetic energies at L_{st} and with $l_{\mathrm{ni,dec},\perp,\mathrm{sup}}$ close to L_{st}, the turbulence anisotropy at $l_{\mathrm{ni,dec},\perp,\mathrm{sup}}$ is insignificant.

Obviously, compared with the super-Alfvénic CNM and MCs, we see that the sub-Alfvénic WNM is more favorable for the formation of profoundly elongated low-density parallel filaments.

3.4. Examples for Low-density Parallel Filaments in the ISM

Perpendicular turbulent mixing of Alfvén modes can account for the formation of low-density parallel filaments in both diffuse warm phases with subsonic to transonic turbulence and dense cold phases with supersonic turbulence. Some examples are as follows.

(1) *H I filaments.* Observations show that filamentary structures in neutral hydrogen (H I) gas with a median column density $N_{\mathrm{H\,I}} \approx 10^{19.1}\,\mathrm{cm}^{-2}$ are aligned with the magnetic field measured by *Planck* (Kalberla et al. 2016; see also Clark et al. 2014, 2015). Here we caution that to extract density structures from channel maps, the velocity dispersion caused by turbulence should be taken into account and thus a sufficient channel spacing should be used (Lazarian 2009). Direction-dependent H I power spectra associated with H I filaments show turbulence anisotropy (Kalberla & Kerp 2016; Kalberla et al. 2017), which we suggest as the origin of low-density parallel filaments. We note that the GS95 turbulence anisotropy is only observable in the reference frame of the local magnetic field (LV99; Cho et al. 2002), which is different from the anisotropy obtained in the global reference frame involving the projection effect.

(2) *Striations in diffuse regions of MCs.* Striations, a network of faint and elongated density structures aligned along the magnetic field, are found in the low-column density ($N_H \approx (1\text{–}2) \times 10^{21}\,\mathrm{cm}^{-2}$) regions in MCs (Goldsmith et al. 2008; Heyer et al. 2016). The high velocity gradient transverse to the magnetic field compared to that along the field direction (Heyer et al. 2008) and the spatial power spectrum transverse to the magnetic field (Tritsis & Tassis 2016) provide strong observational evidence for anisotropic turbulent mixing as the mechanism of their formation.

(3) *Subfilaments in MCs.* Subfilaments are the striations perpendicular and connected to the main filaments, which can contribute to the growth of main filaments through the mass accretion along them (Goldsmith et al. 2008; Schneider et al. 2010; Hennemann et al. 2012; Palmeirim et al. 2013). In this

Table 1
Parameters in Different Partially Ionized Interstellar Phases

	n_H (cm^{-3})	n_e/n_H	B_0 (μG)	T (K)	$\mathcal{M}_s$	$\mathcal{M}_A$	L_{st} (pc)	$l_{\nu,\perp}$ (pc)	$l_{ni,dec,\perp}$ (pc)	A_ν	A_{dec}
WNM	0.4	0.1	5	6000	1.1	0.6	11.1	2.3×10^{-3}	⋯	46.0	⋯
CNM	30	10^{-3}	5	100	8.5	5	0.2	⋯	2.3×10^{-4}	⋯	10.0
MC	300	10^{-4}	5	20	28.9	15.9	7.5×10^{-3}	⋯	9.3×10^{-5}	⋯	4.3

scenario, the velocity distribution within subfilaments is mainly regulated by gravitational infall instead of turbulent mixing.

4. Formation of Dense Filaments in Supersonic Interstellar Turbulence

In cold MCs, the turbulence is highly supersonic (Zuckerman & Palmer 1974; Larson 1981; Heyer & Brunt 2004). Apart from the low-density parallel filaments induced by the perpendicular mixing of Alfvénic turbulence (Section 3), a network of shocks driven by supersonic turbulent flows generate significant density enhancements (Mac Low & Klessen 2004; Padoan et al. 2004; Kowal et al. 2007). The shock compression deforms the spectrum of density fluctuations to be different from that of turbulent velocities (Beresnyak et al. 2005; Kowal et al. 2007) and accounts for the formation of dense filaments in MCs (Mocz & Burkhart 2018; Robertson & Goldreich 2018).[5]

The density contrast across the shock is

$$\frac{\rho_2}{\rho_1} \approx \sqrt{2}\,\mathcal{M}_{A1} \tag{16}$$

when the magnetic pressure dominates in the downstream region, and

$$\frac{\rho_2}{\rho_1} \approx \mathcal{M}_{s1}^2 \tag{17}$$

when the thermal pressure dominates in the downstream region, where ρ_1 and ρ_2 are densities of the upstream and downstream media, $\mathcal{M}_{A1}$ is the shock Alfvén Mach number corresponding to the transverse component of upstream magnetic field, and $\mathcal{M}_{s1}$ is the shock sonic Mach number (see the Appendix for the detailed derivation). The above compression ratios are consistent with earlier studies on isothermal shocks (see, e.g., Draine 2011). In highly supersonic MHD turbulence, the shock-compressed density varies in different turbulence regimes.

(1) $\mathcal{M}_A \gg \mathcal{M}_s \gg 1$. In a weakly magnetized medium, the shock compression in MHD turbulence is similar to that in hydrodynamic turbulence. The resulting density enhancement solely depends on $\mathcal{M}_{s1}(\sim\mathcal{M}_s)$ (Equation (17), see Padoan & Nordlund 2011; Federrath & Banerjee 2015; Federrath 2016; Robertson & Goldreich 2018). We note that the weak magnetic field can be amplified by the downstream turbulence (Xu & Lazarian 2016, 2017a).

(2) $\mathcal{M}_s \gg \mathcal{M}_A > 1$ or $\mathcal{M}_s \gg 1 > \mathcal{M}_A$. In a strongly magnetized medium, Equation (16) applies to the shock compression of an oblique shock. Only for a quasi-parallel shock, Equation (17) can be used for describing the shock-compressed density.

[5] In 3D supersonic turbulence, due to the interaction of density inhomogeneities with multiple shocks and turbulent mixing (Pan & Scannapieco 2010), filamentary structures instead of 2D sheet-like structures are more likely to be generated.

We can clearly see the magnetic effect on the formation of dense filaments. In the weak-field limit, with no preferred shock propagation direction for the density enhancement, the generated filaments with similar densities are randomly orientated. In the strong-field limit, quasi-parallel shocks are more favorable for generating a large density contrast, resulting in dense filaments nearly perpendicular to magnetic fields. The numerical evidence can be found in, e.g., Kowal et al. (2007) and Mocz & Burkhart (2018). The preference on dense perpendicular filaments in observations of MCs (Planck Collaboration et al. 2016a, 2016b) indicates the dominance of magnetic energy over thermal energy. With respect to the turbulent energy, we note that even the turbulence is super-Alfvénic at the large driving scale, the magnetic energy can still exceed the turbulent energy on smaller scales due to the turbulent energy cascade.

In addition, the width of dense filaments can be estimated as the shock propagation distance reduced by the compression ratio. For an oblique filament, the width can be estimated as (Equation (16)),

$$\delta_o \sim \frac{L}{\sqrt{2}\,\mathcal{M}_{A1}}, \tag{18}$$

which depends on the magnetization and the filament orientation. For the densest perpendicular filaments, by assuming a constant compression ratio determined by $\mathcal{M}_{s1}(\sim\mathcal{M}_s)$, we can approximately have the filament width as (Equation (17))

$$\delta_\perp \sim \frac{L}{\mathcal{M}_s^2}, \tag{19}$$

which depends on the compressibility of medium. Provided $L \sim 10$ pc and $\mathcal{M}_s \sim 10$ (Schneider et al. 2013; Henshaw et al. 2016), we find that $\delta_\perp$ is of the order of 0.1 pc, consistent with observations by, e.g., Arzoumanian et al. (2011) and Koch & Rosolowsky (2015).

5. Discussion

Motivated by ample observations of interstellar density filaments, there have been numerous theoretical arguments and numerical experiments on their formation mechanisms (e.g., Lazarian 1993; Hennebelle 2013; Ntormousi et al. 2014; Smith et al. 2014, 2016; Federrath 2016; Inoue & Inutsuka 2016; Banda-Barragán et al. 2018). In this work, based on the fundamental dynamics of Alfvénic turbulence, we propose a formation mechanism of low-density parallel filaments in the ISM.

Cold H I filaments in the WNM. Based on numerical studies, Saury et al. (2014) argued that the dynamics of the WNM and the CNM are tightly coupled, and the velocity dispersion between CNM clumps is close to the velocity dispersion within the extended WNM. It implies that the denser CNM embedded in the diffuse WNM is dynamically mixed by the turbulent

velocities in the WNM, and thus the cold H I filaments are aligned with the turbulent magnetic fields in the WNM (Kalberla et al. 2016). In this scenario, the elongation of cold H I filaments is determined by the turbulence anisotropy in the WNM (see Section 3.3). The single-phase MHD simulations performed in this work are inadequate to capture the distinctive turbulence properties of the WNM and CNM and their interactions. As we have mentioned, to fully understand the turbulence dynamics in the multiphase ISM, a model for (at least) two-phase MHD turbulence should be applied.

Gravitational effects on dense filaments in MCs. Dense filaments can form in supersonic turbulence without gravity, instead they are the seeds of gravitationally collapsing regions (e.g., Federrath & Klessen 2013; Mocz & Burkhart 2018; Robertson & Goldreich 2018). Dense filaments in MCs set up the necessary condition for the self-gravity to take over the gas dynamics and initiate the subsequent star formation. Gravitational effects, which were not considered in this work, can redistribute the spatial structure of striations, narrow the filament width, and change the velocity distribution and magnetic field orientation within filaments (Ching et al. 2017).

Relation of density filaments to the density gradient (DG) and velocity gradient (VG). For a filamentary density structure, the DG is perpendicular to its major axis. Accordingly, the DG of a parallel filament is perpendicular to the magnetic field $\boldsymbol{B}$, while that of a perpendicular filament is parallel to $\boldsymbol{B}$. In good agreement with our analysis, Yuen & Lazarian (2017b) found that DGs measured in H I gas are perpendicular to $\boldsymbol{B}$, and Yuen & Lazarian (2017a) showed DGs parallel to $\boldsymbol{B}$ at shocks. But we caution that the DG is not always a good indicator of density filaments. For instance, DGs parallel to $\boldsymbol{B}$ can also arise in a gravitationally collapsing region. On the other hand, due to the perpendicular turbulent mixing (Section 3.1), the VG of Alfvénic turbulence is perpendicular to $\boldsymbol{B}$ (González-Casanova & Lazarian 2017). The low-density parallel filaments and the perpendicular VGs observed in both H I gas and MCs (Yuen & Lazarian 2017b; Lazarian & Yuen 2018) have the same physical origin.

It is also important to note that in channel maps with a small channel spacing, the intensity fluctuations are mostly influenced by velocity fluctuations. Density filaments can only be extracted from sufficiently thick velocity channel maps (Lazarian & Pogosyan 2000; Lazarian & Yuen 2018).

6. Summary

The pervasive magnetized turbulence is responsible for the formation of ubiquitous density filaments in the ISM. Corresponding to different turbulence regimes in different interstellar phases, the resulting filaments have distinctive features. Our main results are summarized as follows.

Based on our theoretical understanding of MHD turbulence and numerical experiments, we showed that in compressible MHD turbulence, the perpendicular mixing by Alfvénic turbulence gives rise to low-density filaments aligned with the local magnetic field, which explains the low-density parallel filaments observed in diffuse interstellar media and low-density regions of MCs. The filament elongation depends on the anisotropy of Alfvénic turbulence and varies in different turbulence regimes. More elongated low-density parallel filaments are expected in magnetic energy-dominated turbulence. In the CNM and MCs, the minimum width of a low-density parallel filament is determined by the perpendicular neutral–ion decoupling scale.

In the highly supersonic MHD turbulence in MCs, shock compression generates dense filaments. The filament width depends on the relative importance between magnetic and thermal energies, as well as shock propagation direction.

S.X. acknowledges the support for Program number HST-HF2-51400.001-A provided by NASA through a grant from the Space Telescope Science Institute, which is operated by the Association of Universities for Research in Astronomy, Incorporated, under NASA contract NAS5-26555. S.X. also thanks Chris McKee for useful conversations. S.J. acknowledges the support from the Sherman Fairchild Fellowship at Caltech. A.L. acknowledges the support from grant NSF DMS 1622353. Simulations were performed on Blue Waters supercomputer at NCSA, under the allocation PRAC NSF.1713353 supported by NSF. We have made use of NASA's Astrophysics Data System and the yt astrophysics analysis software suite (Turk et al. 2010).

Appendix
Shock Compression in Highly Supersonic MHD Turbulence

In the rest frame of the shock, the quantities across the shock are related by the jump conditions, which include the conservation of mass,

$$\rho_1 u_1 = \rho_2 u_2, \tag{20}$$

the conservation of momentum,

$$\rho_1 c_1^2 + \rho_1 u_1^2 + \frac{B_1^2}{8\pi} = \rho_2 c_2^2 + \rho_2 u_2^2 + \frac{B_2^2}{8\pi}, \tag{21}$$

and the conservation of magnetic flux

$$B_1 u_1 = B_2 u_2, \tag{22}$$

where ρ_1, u_1, c_1, and B_1 are the mass density, fluid velocity (in the shock propagation direction), the sound speed, and the strength of the transverse magnetic field in the upstream region, and ρ_2, u_2, c_2, and B_2 are those in the downstream region.

Under the consideration of highly supersonic turbulence, Equation (21) is approximately

$$\rho_1 u_1^2 + \frac{B_1^2}{8\pi} \approx \rho_2 c_s^2 + \rho_2 u_2^2 + \frac{B_2^2}{8\pi}. \tag{23}$$

Here we also assume that the shock is isothermal with $c_1 = c_2 = c_s$ due to the efficient cooling in MCs (see, e.g., Whitworth & Clarke 1997). In combination with Equations (20) and (22), the above equation becomes

$$\left(1 - \frac{V_{A2}^2}{2u_1^2}\right) u_2^2 - u_1 u_2 + c_s^2 + \frac{V_{A2}^2}{2} \approx 0, \tag{24}$$

as a quadratic equation of u_2, where $V_{A2} = B_2/\sqrt{4\pi\rho_2}$. Its solutions are:

$$u_2 \approx \frac{u_1 \pm u_1\sqrt{1 - 4\left(1 - \frac{V_{A2}^2}{2u_1^2}\right)\left(\frac{c_s^2}{u_1^2} + \frac{V_{A2}^2}{2u_1^2}\right)}}{2 - \frac{V_{A2}^2}{u_1^2}}. \tag{25}$$

Based on this general form, we next discuss the shock compression in the following two cases:

Case 1: Magnetic-pressure-dominated downstream medium

At $c_s^2 \ll V_{A2}^2$, Equation (25) can be simplified as

$$u_2 \approx \frac{u_1 \pm u_1\left(1 - \frac{V_{A2}^2}{u_1^2}\right)}{2}, \tag{26}$$

where $V_{A2}^2/u_1^2 \ll 1$ should be satisfied. We consider the solution corresponding to nonnegligible compression of the shocked material and obtain,

$$u_2 \approx \frac{V_{A2}^2}{2u_1}. \tag{27}$$

From Equations (20) and (22), we find $V_{A2}^2 = (\rho_2/\rho_1)V_{A1}^2$, where $V_{A1} = B_1/\sqrt{4\pi\rho_1}$, and that the relation in Equation (27) determines the density contrast across the shock as

$$\frac{\rho_2}{\rho_1} \approx \sqrt{2}\frac{u_1}{V_{A1}} = \sqrt{2}\mathcal{M}_{A1}, \tag{28}$$

where $\mathcal{M}_{A1}$ is the shock Alfvén Mach number corresponding to the transverse component of upstream magnetic field.

Case 2: Thermal-pressure-dominated downstream medium

At $c_s^2 \gg V_{A2}^2$, the solutions in Equation (25) can be reduced to

$$u_2 \approx \frac{u_1 \pm u_1\sqrt{1 - \frac{4c_s^2}{u_1^2}}}{2}. \tag{29}$$

We again only consider the situation with a significant compression and find

$$u_2 \approx \frac{c_s^2}{u_1} \tag{30}$$

for a supersonic u_1. Combining the above expression with Equation (20) yields

$$\frac{\rho_2}{\rho_1} \approx \frac{u_1^2}{c_s^2} = \mathcal{M}_{s1}^2, \tag{31}$$

where $\mathcal{M}_{s1}$ is the shock sonic Mach number.

ORCID iDs

Siyao Xu https://orcid.org/0000-0002-0458-7828
Suoqing Ji https://orcid.org/0000-0001-9658-0588

References

André, P., Di Francesco, J., Ward-Thompson, D., et al. 2014, in Protostars and Planets VI, ed. H. Beuther et al. (Tucson, AZ: Univ. Arizona Press), 27
André, P., Men'shchikov, A., Bontemps, S., et al. 2010, A&A, 518, L102
Armstrong, J. W., Rickett, B. J., & Spangler, S. R. 1995, ApJ, 443, 209
Arzoumanian, D., André, P., Didelon, P., et al. 2011, A&A, 529, L6
Balsara, D., & Pouquet, A. 1999, PhPl, 6, 89
Balsara, D. S. 1996, ApJ, 465, 775
Banda-Barragán, W. E., Federrath, C., Crocker, R. M., & Bicknell, G. V. 2018, MNRAS, 473, 3454
Beck, R., Brandenburg, A., Moss, D., Shukurov, A., & Sokoloff, D. 1996, ARA&A, 34, 155
Beresnyak, A., Lazarian, A., & Cho, J. 2005, ApJL, 624, L93
Burkhart, B., Collins, D. C., & Lazarian, A. 2015a, ApJ, 808, 48
Burkhart, B., Falceta-Gonçalves, D., Kowal, G., & Lazarian, A. 2009, ApJ, 693, 250
Burkhart, B., Lazarian, A., Balsara, D., Meyer, C., & Cho, J. 2015b, ApJ, 805, 118
Burkhart, B., Lazarian, A., & Gaensler, B. M. 2012, ApJ, 749, 145
Burkhart, B., Stanimirović, S., Lazarian, A., & Kowal, G. 2010, ApJ, 708, 1204
Chepurnov, A., & Lazarian, A. 2010, ApJ, 710, 853
Chepurnov, A., Lazarian, A., Stanimirović, S., Heiles, C., & Peek, J. E. G. 2010, ApJ, 714, 1398
Ching, T.-C., Lai, S.-P., Zhang, Q., et al. 2017, ApJ, 838, 121
Cho, J., & Lazarian, A. 2002, PhRvL, 88, 245001
Cho, J., & Lazarian, A. 2003, MNRAS, 345, 325
Cho, J., Lazarian, A., & Vishniac, E. T. 2002, ApJ, 564, 291
Clark, S. E., Hill, J. C., Peek, J. E. G., Putman, M. E., & Babler, B. L. 2015, PhRvL, 115, 241302
Clark, S. E., Peek, J. E. G., & Putman, M. E. 2014, ApJ, 789, 82
Collins, D. C., Kritsuk, A. G., Padoan, P., et al. 2012, ApJ, 750, 13
Draine, B. T. 2011, Physics of the Interstellar and Intergalactic Medium (Princeton, NJ: Princeton Univ. Press)
Draine, B. T., & Lazarian, A. 1998, ApJL, 494, L19
Draine, B. T., Roberge, W. G., & Dalgarno, A. 1983, ApJ, 264, 485
Federrath, C. 2016, MNRAS, 457, 375
Federrath, C., & Banerjee, S. 2015, MNRAS, 448, 3297
Federrath, C., & Klessen, R. S. 2012, ApJ, 761, 156
Federrath, C., & Klessen, R. S. 2013, ApJ, 763, 51
Federrath, C., Roman-Duval, J., Klessen, R., Schmidt, W., & Mac Low, M.-M. 2010, A&A, 512, A81
Fryxell, B., Olson, K., Ricker, P., et al. 2000, ApJS, 131, 273
Gaensler, B. M., Haverkorn, M., Burkhart, B., et al. 2011, Natur, 478, 214
Goldreich, P., & Sridhar, S. 1995, ApJ, 438, 763
Goldsmith, P. F., Heyer, M., Narayanan, G., et al. 2008, ApJ, 680, 428
González-Casanova, D. F., & Lazarian, A. 2017, ApJ, 835, 41
Haffner, L. M., Reynolds, R. J., & Tufte, S. L. 1999, ApJ, 523, 223
Hennebelle, P. 2013, A&A, 556, A153
Hennebelle, P., & Falgarone, E. 2012, A&ARv, 20, 55
Hennemann, M., Motte, F., Schneider, N., et al. 2012, A&A, 543, L3
Henshaw, J. D., Longmore, S. N., Kruijssen, J. M. D., et al. 2016, MNRAS, 457, 2675
Heyer, M., Goldsmith, P. F., Yıldız, U. A., et al. 2016, MNRAS, 461, 3918
Heyer, M., Gong, H., Ostriker, E., & Brunt, C. 2008, ApJ, 680, 420
Heyer, M. H., & Brunt, C. M. 2004, ApJL, 615, L45
Hill, A. S., Benjamin, R. A., Kowal, G., et al. 2008, ApJ, 686, 363
Inoue, T., & Inutsuka, S.-I. 2016, ApJ, 833, 10
Kalberla, P. M. W., & Kerp, J. 2016, A&A, 595, A37
Kalberla, P. M. W., Kerp, J., Haud, U., et al. 2016, ApJ, 821, 117
Kalberla, P. M. W., Kerp, J., Haud, U., & Haverkorn, M. 2017, A&A, 607, A15
Koch, E. W., & Rosolowsky, E. W. 2015, MNRAS, 452, 3435
Könyves, V., André, Ph., Men'shchikov, A., et al. 2015, A&A, 584, A91
Kowal, G., & Lazarian, A. 2010, ApJ, 720, 742
Kowal, G., Lazarian, A., & Beresnyak, A. 2007, ApJ, 658, 423
Kowal, G., Lazarian, A., Vishniac, E. T., & Otmianowska-Mazur, K. 2009, ApJ, 700, 63
Kowal, G., Lazarian, A., Vishniac, E. T., & Otmianowska-Mazur, K. 2012, NPGeo, 19, 297
Kritsuk, A. G., & Norman, M. L. 2004, ApJL, 601, L55
Kulkarni, S. R., & Heiles, C. 1987, in Interstellar Processes, Astrophysics and Space Science Library, Vol. 134, ed. D. J. Hollenbach & H. A. Thronson (Dordrecht: D. Reidel), 87
Larson, R. B. 1981, MNRAS, 194, 809
Lazarian, A. 1993, Ap&SS, 206, 37
Lazarian, A. 2005, in AIP Conf. Ser. 784, Magnetic Fields in the Universe: From Laboratory and Stars to Primordial Structures, ed. E. M. de Gouveia dal Pino, G. Lugones, & A. Lazarian (Melville, NY: AIP), 42
Lazarian, A. 2006, ApJL, 645, L25
Lazarian, A. 2009, SSRv, 143, 357
Lazarian, A., Esquivel, A., & Crutcher, R. 2012, ApJ, 757, 154
Lazarian, A., Kowal, G., & Beresnyak, A. 2008, in ASP Conf. Ser. 385, Numerical Modeling of Space Plasma Flows, ed. N. V. Pogorelov, E. Audit, & G. P. Zank (San Francisco, CA: ASP), 3
Lazarian, A., & Pogosyan, D. 2000, ApJ, 537, 720
Lazarian, A., & Vishniac, E. T. 1999, ApJ, 517, 700
Lazarian, A., Vishniac, E. T., & Cho, J. 2004, ApJ, 603, 180
Lazarian, A., & Yan, H. 2014, ApJ, 784, 38
Lazarian, A., & Yuen, K. H. 2018, ApJ, 853, 96
Lee, D. 2013, JCoPh, 243, 269

Lithwick, Y., & Goldreich, P. 2001, ApJ, 562, 279
Mac Low, M.-M., & Klessen, R. S. 2004, RvMP, 76, 125
Maron, J., & Goldreich, P. 2001, ApJ, 554, 1175
Marsh, K. A., Kirk, J. M., André, P., et al. 2016, MNRAS, 459, 342
McClure-Griffiths, N. M., Dickey, J. M., Gaensler, B. M., Green, A. J., & Haverkorn, M. 2006, ApJ, 652, 1339
McKee, C. F., & Ostriker, E. C. 2007, ARA&A, 45, 565
Mocz, P., & Burkhart, B. 2018, MNRAS, 480, 3916
Mouschovias, T. C. 1991, ApJ, 373, 169
Ntormousi, E., Fierlinger, K., Burkert, A., & Heitsch, F. 2014, in IAU Symp. 296, Supernova Environmental Impacts, ed. A. Ray & R. A. McCray (Cambridge: Cambridge Univ. Press), 282
Ntormousi, E., Hennebelle, P., André, P., & Masson, J. 2016, A&A, 589, A24
Padoan, P., Jimenez, R., Nordlund, Å., & Boldyrev, S. 2004, PhRvL, 92, 191102
Padoan, P., & Nordlund, Å. 2011, ApJ, 730, 40
Palmeirim, P., André, P., Kirk, J., et al. 2013, A&A, 550, A38
Pan, L., & Scannapieco, E. 2010, ApJ, 721, 1765
Planck Collaboration, Adam, R., Ade, P. A. R., et al. 2016a, A&A, 586, A135
Planck Collaboration, Ade, P. A. R., Aghanim, N., et al. 2016b, A&A, 586, A138
Qian, L., Li, D., Gao, Y., Xu, H., & Pan, Z. 2018, ApJ, 864, 116
Robertson, B., & Goldreich, P. 2018, ApJ, 854, 88
Santos-Lima, R., Lazarian, A., de Gouveia Dal Pino, E. M., & Cho, J. 2010, ApJ, 714, 442
Saury, E., Miville-Deschênes, M.-A., Hennebelle, P., Audit, E., & Schmidt, W. 2014, A&A, 567, A16
Schneider, N., André, P., Könyves, V., et al. 2013, ApJL, 766, L17
Schneider, N., Csengeri, T., Bontemps, S., et al. 2010, A&A, 520, A49
Schneider, S., & Elmegreen, B. G. 1979, ApJS, 41, 87
Shu, F. H. 1992, The Physics of Astrophysics. Volume II: Gas Dynamics (Mill Valley, CA: Univ. Science Books)
Smith, R. J., Glover, S. C. O., & Klessen, R. S. 2014, MNRAS, 445, 2900
Smith, R. J., Glover, S. C. O., Klessen, R. S., & Fuller, G. A. 2016, MNRAS, 455, 3640
Tritsis, A., & Tassis, K. 2016, MNRAS, 462, 3602
Turk, M. J., Smith, B. D., Oishi, J. S., et al. 2010, yt: A Multi-Code Analysis Toolkit for Astrophysical Simulation Data, Astrophysics Source Code Library, ascl:1011.022
Tzeferacos, P., Fatenejad, M., Flocke, N., et al. 2012, HEDP, 8, 322
Vranjes, J., & Krstic, P. S. 2013, A&A, 554, A22
Whitworth, A. P., & Clarke, C. J. 1997, MNRAS, 291, 578
Williams, J. P., Blitz, L., & McKee, C. F. 2000, in Protostars and Planets IV, ed. V. Mannings, A. P. Boss, & S. S. Russell (Tucson, AZ: Univ. Arizona Press), 97
Xu, S., & Lazarian, A. 2016, ApJ, 833, 215
Xu, S., & Lazarian, A. 2017a, ApJ, 850, 126
Xu, S., & Lazarian, A. 2017b, NJPh, 19, 065005
Xu, S., Lazarian, A., & Yan, H. 2015, ApJ, 810, 44
Xu, S., Yan, H., & Lazarian, A. 2016, ApJ, 826, 166
Xu, S., & Zhang, B. 2016, ApJ, 824, 113
Xu, S., & Zhang, B. 2017a, ApJL, 846, L28
Xu, S., & Zhang, B. 2017b, ApJ, 835, 2
Yan, H., & Lazarian, A. 2002, PhRvL, 89, B1102
Yuen, K. H., & Lazarian, A. 2017a, arXiv:1703.03026
Yuen, K. H., & Lazarian, A. 2017b, ApJL, 837, L24
Zuckerman, B., & Evans, N. J., II 1974, ApJL, 192, L149
Zuckerman, B., & Palmer, P. 1974, ARA&A, 12, 279